

Contents

1	Introduction	1
2	Theoretical Background	3
2.1	The Shell Model	3
2.2	The Nilsson Model	6
2.3	Coulomb Effects and Mirror Symmetry	8
3	Experimental Techniques	11
3.1	Fusion-Evaporation Reactions	11
3.2	Gamma-Ray Detectors	13
3.3	Ancillary Detectors	15
3.3.1	Microball	15
3.3.2	Neutron Shell	16
4	Data Handling	17
4.1	Compression	17
4.2	Presorting	18
4.2.1	Proton- α discrimination	18
4.2.2	Neutron- γ discrimination	18
4.2.3	Suppression of false two-neutron events	21
4.2.4	Efficiency of the Neutron Shell	21
4.2.5	The event-by-event reconstruction method	22
4.3	Sorting	26
4.3.1	TE gating	26
5	Data Analysis	28
5.1	Coincidence Spectroscopy	28
5.2	Spin and Parity Assignment of Nuclear States	28
5.2.1	Electro magnetic transitions	30
5.2.2	Spin assignment of nuclear states	30
5.2.3	Parity assignment of nuclear states	31
6	Conclusions and Outlook	33
	Acknowledgements	35
	References	37

Chapter 1

Introduction

In 1932 James Chadwick discovered the neutron [1, 2], which is the second building block of the atomic nucleus next to the proton. Later the same year Werner Heisenberg introduced the concept of isospin [3, 4, 5] which suggests that the neutron and proton can be described as two different states of the same particle, the nucleon. Heisenberg proposed a neutron-proton interaction which, besides from a phenomenological spatial part, also depends on spin and isospin of the two particles. This is very much alike the approach as in modern nuclear physics today. It is reasonable, although not completely justified, to require that a nucleon-nucleon potential is rotation invariant in isospin space in the same way as it must be rotation invariant in ordinary space. This immediately implies that the nuclear force is charge independent and that the isospin symmetric neutron-neutron and proton-proton systems are synonymous. However, the Coulomb interaction between protons clearly breaks this symmetry. An additional contribution arises from the mass difference of neutrons and protons. In principal, the most straightforward way to experimentally study the breaking of isospin symmetry would then be to study two-nucleon systems. The problem however, is that the only bound two-nucleon system is the deuteron, ${}^2\text{H}$. Both the neutron-neutron system and ${}^2\text{He}$ are unbound. Although the opposite would be great from isospin studies we should be pleased with the fact that ${}^2\text{He}$ is unbound. Otherwise the p-p burning process in the interior of stars, including our sun, would proceed much faster and the evolution would probably not have had time enough to develop even the simplest forms of life. However, we can still learn something about isospin from ${}^2\text{H}$. The only bound state of ${}^2\text{H}$ is isospin asymmetric. The absence of isospin symmetric states tells us that the nucleon-nucleon potential indeed is isospin dependent and that it seems to favour isospin asymmetric systems. Isospin symmetry breaking can be studied in heavier nuclear systems. This is interesting because Coulomb effects are more pronounced in heavier nuclei since more protons are present. Especially interesting to study are pairs of mirror nuclei, which have the number of protons and neutrons interchanged. The difference in level energies of excited states in these nuclei turns out to be very sensitive to which configurations that are involved. To form nuclear states with increasing spin the valence particles align their spin towards the same direction. To determine which particles that take part in the spin alignment the study of mirror nuclei will help us. In nuclei from ${}^{40}\text{Ca}$ to ${}^{56}\text{Ni}$ the valence particles are mainly occupying the same shell, namely the $1f_{7/2}$ shell. The $1f_{7/2}$ shell is relatively isolated in energy and

situated between the $1d_{3/2}$ shell and the upper fp shell, consisting of the $2p_{3/2}$, $1f_{5/2}$ and $2p_{1/2}$ shells. Therefore, we expect that the wave functions of nuclear states in this region are dominated by $1f_{7/2}$ particle configurations which makes results from mirror symmetry studies easier to interpret. Recently, extensive studies have been performed on mirror nuclei in this shell including the $A = 47$ [6] and $A = 49$ [6, 7] $T_z = \pm 1/2$ nuclei and the $A = 46$ [8] and $A = 50$ [9, 10] $T = 1$ isobaric triplets. A few excited mirror states are known for $A = 53$ [11] and $A = 55$ [12]. Along with the experimental advances it is now also possible to perform large-scale shell-model calculations up to $A = 52$ [13]. Thus to reproduce Coulomb effects in $1f_{7/2}$ mirror nuclei is really a test for the nuclear shell model.

This thesis focuses on the $A = 51$ mirror nuclei. This is the heaviest mirror system for which extensive studies have been performed. It is based on the following publications:

1. **The $A = 51$ Mirror Nuclei ^{51}Fe and ^{51}Mn**

J. Ekman, D. Rudolph, C. Fahlander, R.J. Charity, W. Reviol, D.G. Sarantites, V. Tomov, R.M. Clark, M. Cromaz, P. Fallon, A.O. Macchiavelli, M. Carpenter, and D. Seweryniak,
Eur. Phys. J. A **9**, 13 (2000).

2. **The $A = 51$ Mirror Nuclei ^{51}Fe and ^{51}Mn**

J. Ekman, D. Rudolph, C. Fahlander, R.J. Charity, W. Reviol, D.G. Sarantites, V. Tomov, R.M. Clark, M. Cromaz, P. Fallon, A.O. Macchiavelli, M. Carpenter, and D. Seweryniak,
Proceedings *Pingst 2000, Selected Topics on $N = Z$ Nuclei*, June 2000, Lund, Sweden, Eds. D. Rudolph and M. Hellström, Bloms i Lund AB, p. 232.

Chapter 2

Theoretical Background

2.1 The Shell Model

The atomic nucleus is built up by protons and neutrons, referred to as nucleons, which form a quantal many-body system. Nucleons are fermions, that is they are spin 1/2- particles and therefore must obey the Pauli principle. Empirically we know that nuclei exhibit a shell structure in a similar way as atoms. One experimental evidence of this is that the two-neutron separation energies show discontinuities at certain neutron numbers, namely at 2, 8, 20, 28, 50, 82, and 126. These numbers are the so-called *magic numbers*.

A natural starting point for a theoretical model to understand this behaviour is to solve the Schrödinger equation with the Hamiltonian for an A -particle system

$$H = \sum_{i=1}^A \left(-\frac{\hbar^2}{2m} \nabla_i^2 \right) + \frac{1}{2} \sum_{i \neq j}^A v(\vec{r}_i, \vec{r}_j) \quad (2.1)$$

The left term in the Hamiltonian describes the kinetic energy of the nucleons. The right term describes the interaction between all nucleons in the nucleus. The total wave function of the system is then the product of the single-particle wave functions, properly normalised and antisymmetrised. The facts that we are dealing with a finite many-body system, and that the interaction between the particles is not fully understood make things complicated. To avoid these problems we approximate the nuclear interaction term in Eq. 2.1 with an average central potential. This average potential is chosen such that any residual interaction required to describe the nucleus is minimised. Since the nuclear force is a short-range interaction, the central potential is, to a first approximation, proportional to the density distribution of the nucleus. The latter is well known for a wide range of stable nuclei from electron scattering experiments. One central potential that is often used is the Woods-Saxon potential

$$V_{WS}(r) = \frac{-V_0}{1 + e^{\frac{r-R}{a}}} \quad (2.2)$$

where the well depth V_0 is of the order of 50 MeV, R is the nuclear radius given by $R = R_0 A^{1/3}$ fm ($R_0 \approx 1.25$ fm), and A is the mass number of the nucleus. The skin diffuseness is represented by the parameter a , which is approximately 0.55 fm.

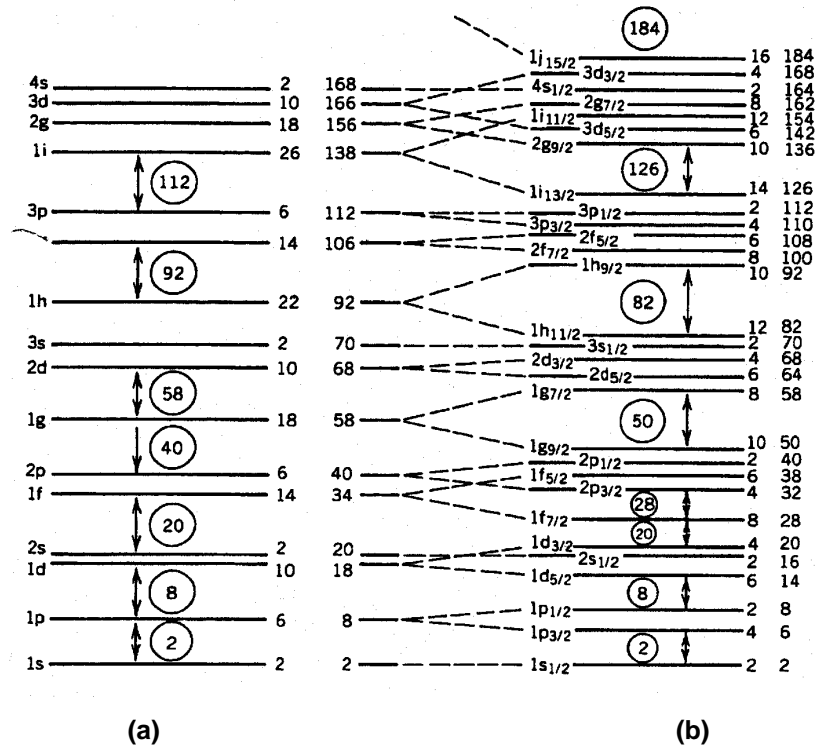


Figure 2.1: Single-particle energies calculated with a Woods-Saxon potential without spin-orbit coupling (a) and with spin-orbit coupling (b). The degeneracy of each level and the cumulate number of nucleons up to that level is shown to the right of each figure. Numbers in circles are the magic numbers. Picture taken from Ref. [14].

The Schrödinger equation for such a central potential can be separated into a radial part and an angular part. The solution of the angular part is independent of the central potential. To solve it, a quantum number l is introduced, which is related to the orbital angular momentum \vec{l} as $\vec{l}^2|\psi\rangle = l(l+1)\hbar^2|\psi\rangle$, where $|\psi\rangle$ is the single-particle wave function. The l quantum-number can only take integer values and is often denoted as s, p, d, f, g, etc. corresponding to $l = 0, 1, 2, 3, 4$, etc. Another important quantum-number is the parity π , which reflects the symmetry of the wave function when the signs of the spatial coordinates are interchanged. A state with an even l -value has positive parity, and a state with odd l has negative parity. The orbital angular momentum vector has different directions in space with respect to the quantisation axis z , and the projection of \vec{l} on the z -axis is given by $l_z|\psi\rangle = m_l\hbar|\psi\rangle$, where m_l can take values $l, l-1, \dots, l=0, \dots, -l+1, -l$. Nucleons also have intrinsic spin \vec{s} , and the projection on the z -axis is given by $s_z|\psi\rangle = m_s\hbar|\psi\rangle$, where $m_s = \pm 1/2$. The degeneracy of a state, i.e., the number of particles that can occupy a state with a given energy, is $2(2l+1)$, where the factor 2 comes from the two directions that the intrinsic spin can take. Another quantum number is the principal quantum number n , which is the number of nodes the radial wave function has. The energy eigenvalues obtained when solving the Hamiltonian with a Woods-Saxon potential can be seen in Fig. 2.1(a); A Woods-Saxon potential alone does not reproduce the observed magic numbers beyond 20. To solve this problem it is necessary to add the so-called spin-orbit interaction. The modified Woods-Saxon

potential can then be expressed as

$$V_{MWS}(r) = \frac{-V_0}{1 + e^{\frac{r-R}{a}}} + V_{SO}(r)\vec{l} \cdot \vec{s} \quad (2.3)$$

The last term in the equation, the spin-orbit interaction, couples the orbital angular momentum \vec{l} to the intrinsic spin \vec{s} to form a total angular momentum (or spin) \vec{j} . Similar to \vec{l} , \vec{j} is associated with quantum numbers j and $m_j = m_l + m_s$. A consequence of the spin-orbit interaction is that it splits the degeneracy of each $l > 0$ level into a $j = l + 1/2$ and a $j = l - 1/2$ level in such a way that the $j = l + 1/2$ level is lowered in energy. The energy levels calculated with the modified Woods-Saxon potential are shown in Fig. 2.1(b). Levels are denoted as nl_j . The degeneracy for each level becomes $2j + 1$ and we see from the figure that the experimental magic numbers are well reproduced. For a more detailed description on the spherical shell model, see for instance Refs. [14, 15].

Using Fig. 2.1(b) we can also predict spins and parities of the ground states of nuclei. Neutrons and protons are treated separately. The fact that two like particles tend to couple to spin zero in ground states, due to the so-called pairing interaction, simplifies things. It implies that all even-even nuclei (even number of protons and neutrons) have spin zero ground states, which is observed experimentally. The total parity of a nucleus is the product of the single-particle parities, and thus the total spin and parity I^π of an even-even nucleus is 0^+ . For odd-even nuclei the spin and parity is determined by the last odd particle. One example is ^{43}Ca where we from Fig. 2.1(b) would infer that the ground-state spin and parity is $7/2^-$, which is also observed experimentally. For odd-odd nuclei, the situation is more complicated since both the last odd proton and neutron contribute with non-zero spin. Therefore, we must couple the spin of the neutron j_n with the spin of the proton j_p to a total spin I . This coupling obeys the following general rule

$$|j_p - j_n| \leq I \leq |j_p + j_n| \quad (2.4)$$

As an example, for ^{42}Sc , with one proton and one neutron in the $f_{7/2}$ orbit, the total spin can be $I = 0, 1, 2, 3, 4, 5, 6$ and, 7. The total parity however is positive. Experimentally the spin and parity of the ground state of ^{42}Sc is 0^+ .

These simple rules do not work for all nuclei. For example, if we would like to predict the ground state spin and parity for ^{51}Mn , an odd-even nucleus, we would predict $7/2^-$, as in the case of ^{43}Ca . However, the spin and parity for ^{51}Mn is experimentally found to be $5/2^-$. This discrepancy tells us that the simple *spherical* shell model does not work for all nuclei. Could it be that ^{51}Mn is not spherical in its ground state?

2.2 The Nilsson Model

Although the spherical shell-model has earned a lot of success in describing low-spin states in spherical nuclei, it fails to describe phenomena in the vast majority of nuclei. We find spherical nuclei in the direct vicinity of double-magic nuclei (both proton and neutron number are magic). Examples are ^{40}Ca ($N = Z = 20$) and ^{56}Ni ($N = Z = 28$). But in a lot of nuclei with many valence particles outside closed shells we observe signatures of deformation.

To understand the fundamental issues of single particles moving in a deformed nucleus, a deformed shell model was developed by S. G. Nilsson in 1955 [16], generally known as the Nilsson model, which will be discussed briefly below. For a more detailed discussion, see Ref. [17].

To model a single particle moving in a deformed nucleus the Deformed Modified-Oscillator (DMO) potential is often used.

$$V_{DMO} = \frac{1}{2}M(\omega_z^2 z^2 + \omega_\perp^2(x^2 + y^2)) - 2\kappa\hbar\omega_0(\vec{l} \cdot \vec{s}) - \kappa\mu\hbar\omega_0(\vec{l}^2 - \langle \vec{l}^2 \rangle_N) \quad (2.5)$$

The first term describes the deformation. ω_z and ω_\perp are the harmonic oscillator frequencies in the z -direction and the directions perpendicular to the z -direction, respectively. It is an axially symmetric term with two axis equal, $\omega_\perp = \omega_x = \omega_y$. For prolate shapes (American football like shape), which we are going to focus on, $\omega_z < \omega_\perp$. We define a deformation parameter δ as

$$\delta = 3 \frac{\omega_\perp - \omega_z}{2\omega_\perp + \omega_z} \quad (2.6)$$

The second term in Eq. 2.5 is the spin-orbit coupling described above. The third term lowers the energy of high- l states to simulate the effect of a potential with surface, for example the Woods-Saxon potential in Eq. 2.2. The parameters κ and μ are determined empirically.

The Schrödinger equation with the DMO potential can be solved in two limits. In the first case it is assumed that the deformation term is small compared to the spin-orbit term. We can then treat the deformation as a perturbation. In this case one-particle states may be approximately described by the spherical quantum-numbers nlj and a good quantum-number Ω , which is the projection of the total angular momentum on the symmetry axis (z -axis).

In the second case we assume that the deformation term is much larger compared to the spin-orbit term. We can then treat the spin-orbit term as a perturbation. The good quantum numbers in the large deformation limit are $N = n_z + n_\perp$, n_z , Λ and Ω . n_z and n_\perp are the number of nodes the wave function takes in the z -direction and the perpendicular directions, respectively. Λ is the projection of the orbital angular momentum on the symmetry axis. These quantum numbers are often referred to as the asymptotic quantum numbers. The parity of a state is given by $\pi = (-1)^N$. Therefore parity is also a good quantum number.

For intermediate values of the deformation the situation is more complicated, since the spin-orbit term mixes levels with different values of n_z , n_\perp , and Λ . However, we still use the asymptotic quantum-numbers to describe single-particle orbits. To solve this eigenvalue problem we must carry out the diagonalisation of the Hamiltonian

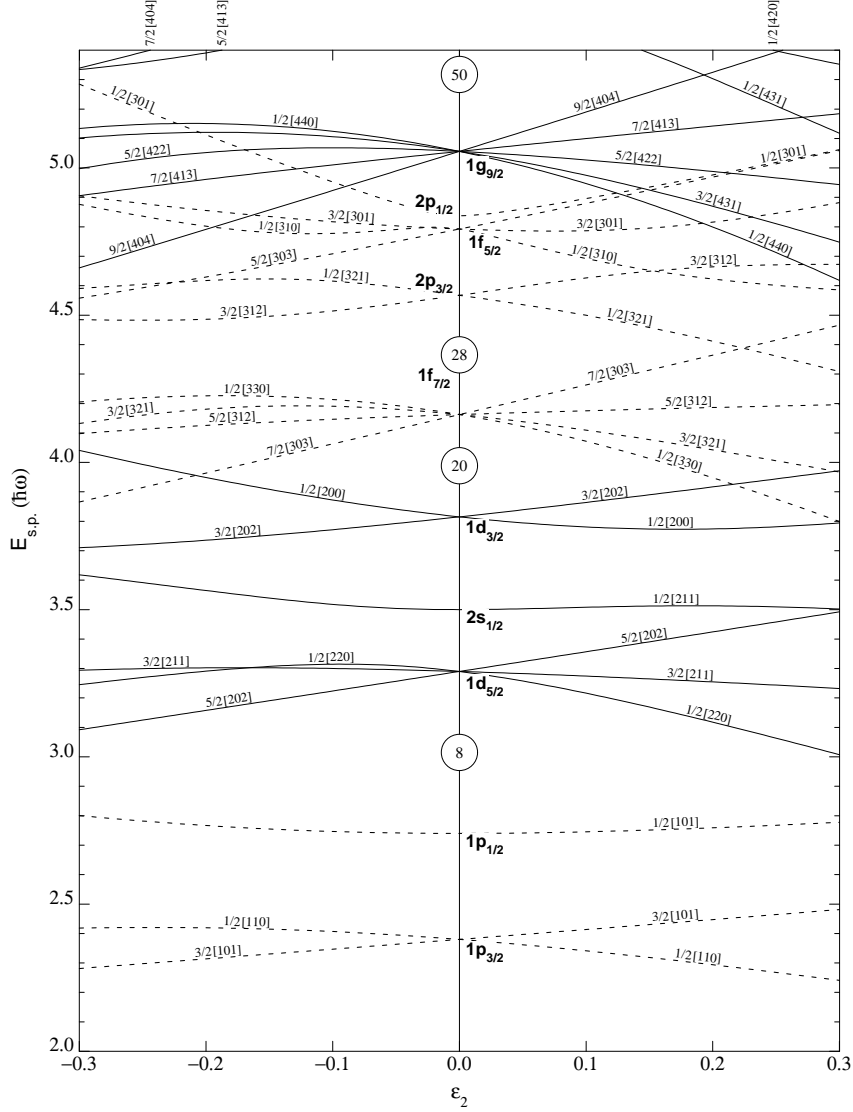


Figure 2.2: Nilsson diagram for protons Z or neutrons N , $Z, N \leq 50$. The deformation parameter $\epsilon_2 = \delta$. Orbits are labelled $\Omega[Nn_z\Lambda]$. Solid (dashed) lines indicate positive (negative) parity states.

with the potential in Eq. 2.5. The result is a Nilsson diagram shown in Fig. 2.2. Due to the axial symmetry of the potential used, there is no way to differ between orbits having for example $\Omega = 3/2$ and $\Omega = -3/2$ and each level is therefore two-fold degenerate. The projection of the total angular momentum on the symmetry axis is given by

$$K = \sum_{i=1}^A \Omega_i \quad (2.7)$$

It is now possible to predict spin and parity of the ground state in deformed nuclei, for example in ^{51}Mn . We simply place two neutrons in each state up to $N = 26$ and two protons in each state up to $Z = 24$. By doing this we end up with a single proton in the $\Omega[Nn_z\Lambda] = 5/2[312]$ orbit, as long as the ground-state deformation is moderate ($\delta \leq 0.3$). The spin and parity of the ground state in ^{51}Mn is predicted to be $I^\pi = K^\pi = 5/2^-$. Experimentally we find that $I^\pi = 5/2^-$ and a deformation

$\delta \approx 0.2$. The Nilsson model describes single-particle motion in deformed nuclei very well.

2.3 Coulomb Effects and Mirror Symmetry

The decisive force in atomic nuclei is the strong nuclear force. However, this is not the only force acting on the nucleons. Since the protons are positively charged the Coulomb force must also be considered. However, if we neglect the Coulomb interaction, the observed properties of neutrons and protons are expected to be very similar. We can then treat the proton and the neutron as being different states of the same particle. Therefore, it is convenient to introduce a quantum number describing these states, namely the isospin quantum-number t . A nucleon has $t = 1/2$ and two possible directions in isospin-space, $t_z = +1/2$ and $t_z = -1/2$, corresponding to a neutron and a proton, respectively. The total isospin projection in a nucleus T_z is given by $T_z = \frac{1}{2}(N - Z)$. Mirror nuclei are a pair of nuclei where the number of protons and neutrons are interchanged. One example is ^{51}Fe and ^{51}Mn , which this thesis focuses on. ^{51}Fe has 26 protons and 25 neutrons and $T_z = -1/2$, whereas ^{51}Mn has 25 protons and 26 neutrons and $T_z = +1/2$.

The Coulomb interaction between two protons can be expressed as

$$V_C = \frac{e^2}{R} \quad (2.8)$$

where e is the charge of the protons and R is the distance between them. To describe the proton single-particle energies, a potential like Eq. 2.8 is often added to a realistic nuclear potential (Eq. 2.3). Coulomb interaction also affects the binding energy and mass of nuclei. The Coulomb energy stored in a uniformly charged sphere, with a total charge Z and radius R_c , can be expressed as

$$E_C = \frac{3}{5} \frac{Z^2 e^2}{R_C} \quad (2.9)$$

If we assume the strong nuclear force to be charge independent, the difference in binding energy of mirror nuclei must equal the difference in Coulomb energy. This Coulomb-energy difference is also known as the Coulomb Displacement Energy (CDE). Since the Coulomb interaction of each proton with itself is already included in the mass of the proton, we must exchange Z^2 with $Z(Z - 1)$ in Eq. 2.9. CDE for $T_z = \pm 1/2$ mirror nuclei becomes

$$CDE = \frac{3}{5} \frac{e^2}{R_C} (2Z - 2) \quad (2.10)$$

If we compare the result from Eq. 2.10 with experimental values, we will find that the CDE is overestimated with about 10%, assuming $R_C = R_0 A^{1/3}$ and $R_0 = 1.22$ fm. This discrepancy is due to skin diffuseness and shell effects, which are not considered in Eq. 2.10. A more realistic expression for the Coulomb energy stored in nuclei is given in Ref. [17] page 16.

$$E_C = \frac{3}{5} \frac{Z(Z - 1)e^2}{R_C} \left(1 - \frac{5\pi^2}{6} \left(\frac{a}{R_c} \right)^2 - \frac{0.76}{Z^{2/3}} \right) \quad (2.11)$$

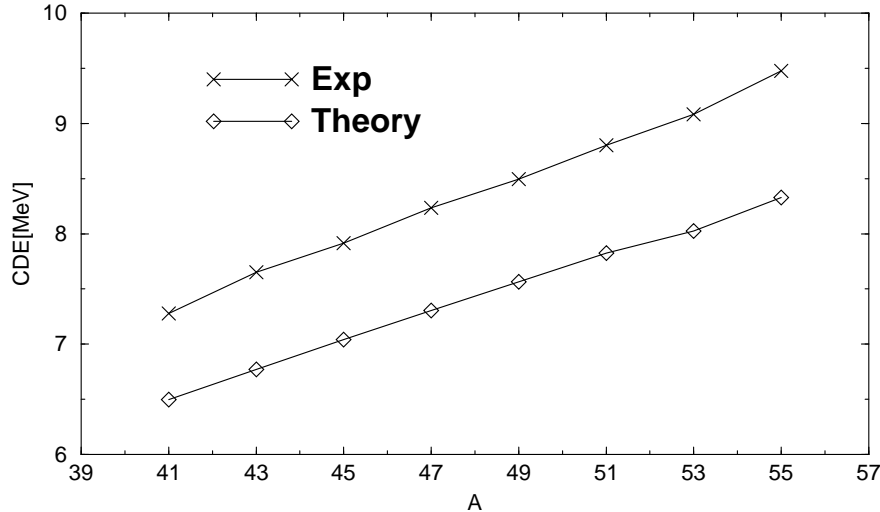


Figure 2.3: Experimental CDE:s compared to CDE:s calculated with Eq. 2.11 for $T_z = \pm 1/2$ mirror nuclei in the $1f_{7/2}$ shell. See text for details.

The second term in the parenthesis is the correction introduced when integrating over a charge distribution with skin diffuseness parameter a (cf Eq. 2.2). The third term, the so-called exchange correction, takes the Pauli principle into consideration. This means that the immediate vicinity of one proton is a forbidden volume for other protons. It is calculated assuming a two-particle density function for the protons. In Fig. 2.3 we compare the CDE:s calculated with Eq. 2.11 using $R_0 = 1.22$ fm and $a = 0.55$ fm, to experimental CDE:s for $T_z = \pm 1/2$ mirror nuclei in the $1f_{7/2}$ shell. We now instead underestimate CDE with about 10%. This is the so called Nolen-Schiffer anomaly [18]. Even when using refined mean-field calculations the anomaly remains. However, recently, claims have been put forward that the problem can be solved without destroying the charge independence of the nuclear force [19]. Instead, a small neutron skin is introduced to get consistency between experimentally observed proton radii and CDE:s.

So far we have only studied Coulomb-energy differences of ground states in mirror nuclei. It is even more interesting to study Coulomb effects of excited states. Theoretically, this cannot be done using a simple model, but we can still learn a lot by studying experimental level schemes. We first determine the difference in level energies of mirror nuclei, i.e., the level energies of the proton-richer partner minus the respective level energies of the neutron-richer partner. Plotted as a function of angular momentum, we obtain the so-called Coulomb Energy Difference (CED)-diagram. Under the assumption that the nuclear force is charge independent, the CED-diagrams should reflect the expectation values of the Coulomb interaction for the particle configurations involved. Figure 2.4(a) shows level schemes and Fig. 2.4(b) shows the CED-diagram for the $T_z = \pm 1$ mirror nuclei ${}^{42}_{22}\text{Ti}$ and ${}^{42}_{20}\text{Ca}$. In the ground state they have two protons and two neutrons in the $f_{7/2}$ -shell outside the doubly-magic ${}^{40}_{20}\text{Ca}$, respectively. The maximum spin that can be created in these configurations is $I = 6$, which corresponds to the full alignment of the proton and neutron pair, respectively. When we break and align the proton pair in ${}^{42}_{22}\text{Ti}$, the average distance between the protons increases. This leads to an increase

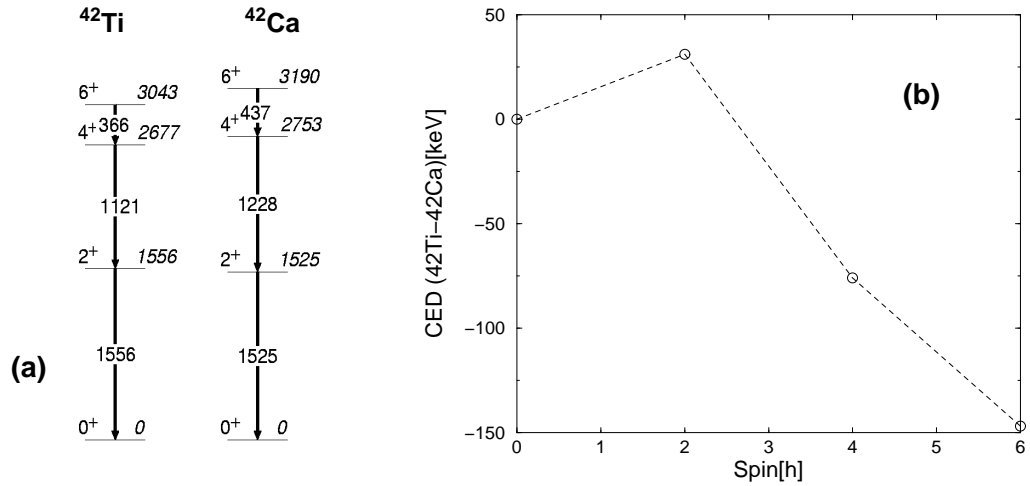


Figure 2.4: Experimental level schemes(a) and corresponding CED-diagram(b) for the $T_z = \pm 1$ mirror nuclei ^{42}Ti and ^{42}Ca .

in binding energy due to the decrease in Coulomb energy. In $^{42}_{20}\text{Ca}$ we do not expect such an effect, since we break and align a pair of neutrons. The net effect should be that the CED decreases with increasing spin, which is also what we observe, except for the increase in CED for the $I = 2$ level.

Chapter 3

Experimental Techniques

3.1 Fusion-Evaporation Reactions

To study high-spin properties in nuclei, it is necessary to use a reaction that generates sufficient angular momentum and excitation energy. A common way to produce high-spin states in $N \approx Z$ nuclei is by using a heavy-ion compound fusion-evaporation reaction. The fusion-evaporation reaction is a multi-step process schematically shown in Fig. 3.1. The projectile nucleus and the target nucleus fuse into a very hot and fast rotating system. It forms a highly excited compound nucleus with the excitation energy E^* expressed as.

$$E^* = Q + E_{CM} \quad (3.1)$$

Q is the Q value of the reaction and E_{CM} is the center-of-mass energy available for excitation given by

$$E_{CM} = T_p \frac{M_t}{M_p + M_t} \quad (3.2)$$

T_p is the beam energy and M_p and M_t are the masses of the projectile nucleus and the target nucleus, respectively. The maximum angular momentum L_{max} that can be given to the compound nucleus is

$$L_{max} = \frac{M_t}{M_p + M_t} \cdot b_{max} \cdot \sqrt{2M_p(T_p - E_C)} \quad (3.3)$$

where b_{max} is the maximum impact parameter which generates such a reaction. It can be estimated by

$$b_{max} = R_p + R_t = R_0(A_p^{1/3} + A_t^{1/3}) \quad (3.4)$$

R_p and A_p (R_t and A_t) are the radius and the mass number of the beam nucleus (target nucleus). We note that the angular momentum of the compound nucleus can take any value between 0 and L_{max} , depending on the impact parameter b . To a first approximation, the probability for a certain angular momentum is proportional to b . Since the projectile nucleus and target nucleus are positively charged, E_{CM} must be larger than the Coulomb barrier E_C which is given by

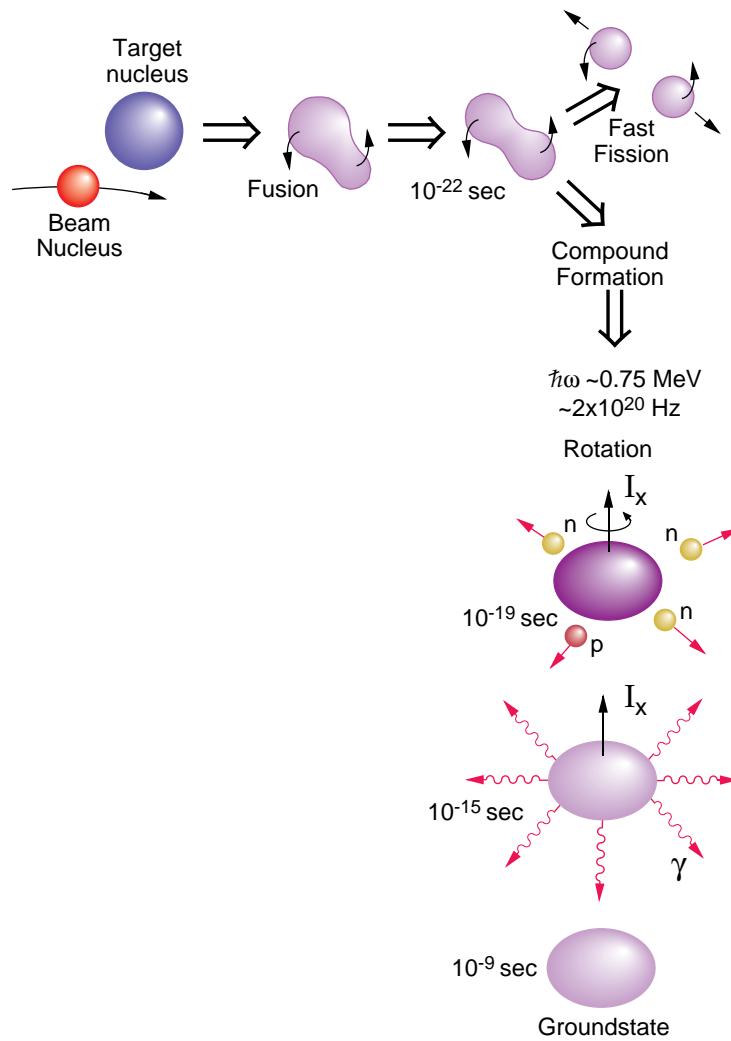


Figure 3.1: Formation and decay of compound nucleus. Taken from Ref. [20].

$$E_C = 1.44 \frac{Z_p Z_t}{R_C} \quad (3.5)$$

where Z_p and Z_t are the proton numbers of the beam nucleus and target nucleus, respectively. R_C is the distance in fm between the target nucleus and projectile nucleus, where the maximal Coulomb barrier is expected, which means $R_C = b_{max}$. As seen in Fig. 3.1, instead of forming a compound nucleus, the fused system may also undergo fast fission. The fission probability depends essentially on how much angular momentum that has been put into the system.

Initially the compound nucleus cools down by evaporating particles, such as neutrons, protons, and α particles (see also Fig. 3.2). This is an efficient cooling process since the evaporated particles take away both binding energy and kinetic energy from the system; α particles take away ~ 15 MeV kinetic energy, protons ~ 10 MeV and neutrons ~ 2 MeV. The evaporated particles also take away angular momentum from the system; α particles $\sim 5-10 \hbar$ and protons and neutrons $\sim 1-2 \hbar$. In the mass $A \sim 60$ region, protons and α particles are much more likely to be evaporated than

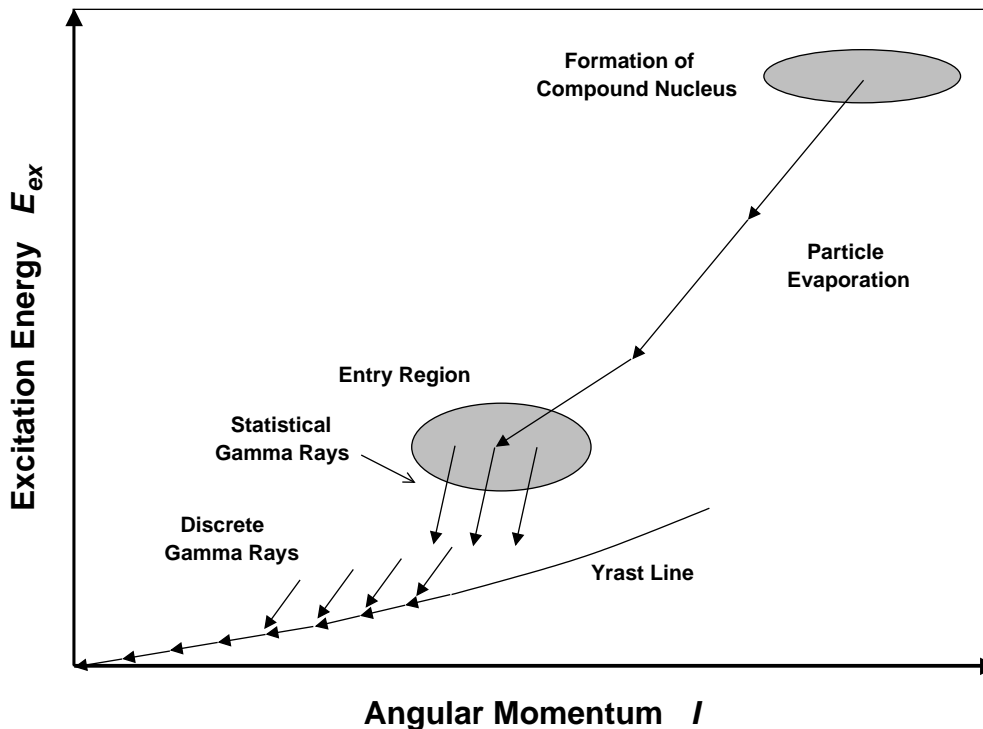


Figure 3.2: Decay of a compound nucleus down to the ground state of a residual nucleus. The excitation energy is plotted vs. angular momentum.

neutrons. This is mainly due to the higher neutron separation energy of ~ 15 MeV, compared to the proton separation-energy of ~ 5 MeV. The number and combination of particles evaporated in each event defines the reaction channel and thus the residual nucleus. Typically a fusion-evaporation reaction in the mass $A \sim 60$ region opens up ~ 20 reaction channels with varying cross sections from tens of μb up to 100 mb. Eventually the evaporation of particles is no longer energetically possible, which happens at about 8 MeV above the *yrast line*¹. Instead the residual nucleus cools down by emitting statistical γ -rays. Finally the residual nucleus decays by emitting discrete γ rays to the ground state. These γ rays carry the information of the structure of the nucleus.

This work is based on data from fusion-evaporation reactions using a 125 MeV ^{32}S beam on a ^{28}Si target, giving the compound nucleus ^{60}Zn . The Q value for this reaction is 6.67 MeV and using Eq. 3.2 we get $E_{CM} \sim 58$ MeV. The excitation energy of the compound nucleus then becomes ~ 65 MeV. Using $R_0=1.25$ fm and $b_{max}=7.76$ fm we get $L_{max} \sim 41 \hbar$.

3.2 Gamma-Ray Detectors

It is necessary to have an efficient γ -ray detection device when studying fusion-evaporation reactions. Since we populate the residual nucleus at high excitation energy, the number of γ rays emitted from one event, the γ -ray multiplicity, can

¹From the Swedish “yrast”, in English “the most dizzy, dizziest”. Refers to the line connecting states with lowest possible energy for a given spin.

be large. In the mass $A \sim 60$ region at $E^* \sim 60$ MeV the γ -ray multiplicity is ~ 15 . This requires that the detection system also has a high energy resolution. High-Purity Germanium (HPGe)-detectors offer extremely good energy resolution (~ 2.0 - 2.5 keV at 1.33 MeV γ -ray energy). To obtain high detection efficiency and granularity it is necessary to use many Ge detectors coupled together in arrays. The two most powerful Ge arrays currently existing are Euroball [21], which is a joint European project and currently located at Institute de Recherches Subatomiques (IReS) in Strasbourg, France, and Gammasphere [22] at the Lawrence Berkeley National Laboratory (LBNL) in Berkeley, U.S.A. This work is based on data from experiments using Gammasphere.

A photo of Gammasphere is shown in Fig. 3.3. It consists of up to 110 Ge-detectors packed in a 4π geometry. The Ge detectors are mounted in 17 rings situated between 17.3° to 162.7° with respect to the beam axis. The front faces of the Ge-detectors are 25 cm from the target location. With this geometry the total photo-peak efficiency is $\sim 9\%$ and the energy resolution is 2.4 keV at 1.33 MeV. For γ energies between 200-1200 keV the Compton-scattering process is the dominating interaction in the Ge crystals. Therefore, γ rays often undergo multiple Compton scattering and escape from the Ge detector thus depositing only part of their energy. This leads to an undesired background. To suppress this background, each Ge detector is surrounded by a shield of BGO crystals². Whenever a γ ray is scattered from the Ge crystal and detected in the BGO shield, it is vetoed and not considered anymore. In this way the ratio of photo-peak events to the total number of events (peak-to-total ratio) is considerably increased. Since the BGO shield is primarily used as a veto detector, the poor energy resolution of BGO does not play a role, but the high efficiency certainly does. If the γ -ray multiplicity is too high, there is a possibility to have γ rays impinging at the BGO shield and the Ge crystal at the same time. In such situations the BGO shield may veto a “good” Ge event. To prevent this, Heavimet³ absorbers are usually placed in front of the BGO shields. In reactions with low γ -ray multiplicity the Heavimet absorbers can be removed, allowing for γ -ray multiplicity and sum-energy measurements, which are discussed in chapter 4.3.1.

The energy resolution for Gammasphere given above is the typical, averaged intrinsic energy resolution of the system obtained if the γ -emitting source is at rest. In fusion-evaporation reactions using thin targets and no backing material to stop the recoiling nuclei, we have to consider kinematical Doppler effects. This will worsen the energy resolution, but can to a large extent be corrected for using an event-by-event reconstruction method described in chapter 4.2.5.

In the two experiments which this work is based on the linear accelerator at Argonne National Laboratory (ANL) in Argonne, U.S.A. and the 88-inch cyclotron at LBNL provided the ^{32}S beam. Both accelerators are operated in pulsed beam mode. The time between pulses for the 88-inch cyclotron was 80 ns. This provides a time calibration for the Ge time spectra as well as a time reference for pulse shape analysis techniques, see chapter 4.2.2.

² $\text{Bi}_4\text{Ge}_3\text{O}_{12}$

³A Ta-Ni-Cu alloy with a density of ≈ 19 g/cm³

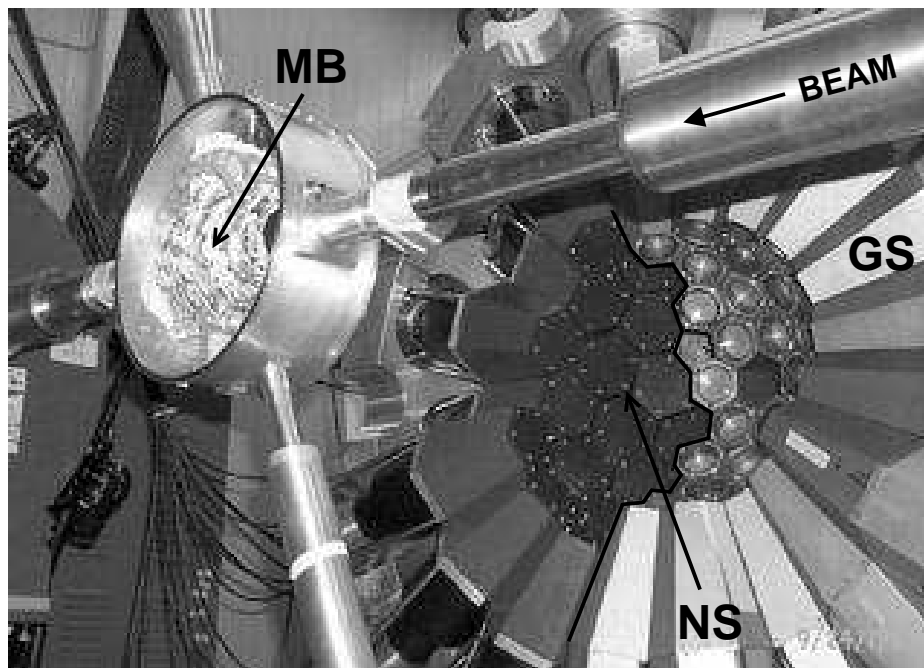


Figure 3.3: One hemisphere of Gammasphere (GS) together with Neutron Shell (NS) and Microball (MB), mounted inside the target chamber. The beam is coming from the right in the picture. Taken from Ref. [23].

3.3 Ancillary Detectors

As stated above fusion-evaporation reactions open up a lot of reaction channels with varying cross sections. As a consequence a raw ungated Ge-spectrum contains a huge amount of γ -ray transitions from many different residual nuclei. This is a problem, especially in the search for nuclei populated in very weak reaction channels. To solve this problem we detect the evaporated particles in coincidence with the emitted γ rays. This provides much cleaner spectra and also the possibility to identify γ -ray transitions of a specific residual nucleus. To detect the evaporated particles, different ancillary detectors can be operated together with Gammasphere. Two of them will be discussed below, namely Microball [24], used for the detection of evaporated light charged particles, and the Neutron Shell [25], used for the detection of evaporated neutrons.

3.3.1 Microball

Microball is situated inside Gammasphere, see Fig. 3.3. It has a large solid angle coverage and provides good particle identification. It also has a small mass to minimise absorption of the γ rays. A high segmentation is also important not to allow too high count rates in individual detectors. To perform sum-energy measurements and charged-particle spectroscopy a good energy resolution is also required.

Microball consists of 95 closely packed CsI(Tl) scintillators, covering 97% of the solid angle. The scintillators are mounted in 9 rings covering the angles from 4° to

171° with respect to the beam axis. Due to the reaction kinematics the evaporated particles are focused at forward angles. Therefore, the most forward rings of Microball are placed at larger distances from the target to reduce count rates because of increased granularity. The target-to-detector distance varies from 45-50 mm in the backward and mid angles up to 110 mm in the most forward ring. The intrinsic energy resolution is 240 keV for 8.78 MeV α particles. The front surface of each detector is covered by Pb or Sn absorber foils in order to stop elastically scattered beam particles.

3.3.2 Neutron Shell

The most proton rich nuclei are populated in reaction channels involving evaporated neutrons. When we produce mirror nuclei, the $T_z = -1/2$ partner is always populated in a neutron channel, assuming stable $N = Z$ target and $N = Z$ projectile combinations. Therefore we are often interested in detecting and identifying the evaporated neutrons.

The detection of neutrons is, however, more complicated than the detection of charged particles. This is due to the different interaction mechanism involved when the particles are passing through matter. Charged particles interact mainly through electro magnetic processes and interactions take place continuously along the tracks. Since neutrons are neutral the dominating interacting with matter in the MeV region is through nuclear scattering. The recoil nucleus then interacts electromagnetically and can be detected. To have neutrons transfer as much energy as possible, a hydrogen-rich material is often used as detector material. From a detection point of view, there are several problems associated with neutron scattering. First of all, the nuclear interactions take place rarely, and therefore many and large detectors are often used. This also means that with some probability a neutron is scattered from one detector to adjacent detectors. As a consequence, false two-neutron events are common. For a description on how these events can be suppressed, see chapter 4.2.3 and Ref. [26].

The Neutron Shell, shown in Fig. 3.3, consists of 30 hexagonal liquid scintillators. When operated together with Gammasphere it replaces the four most forward Ge rings and covers $\sim 25\%$ of the solid angle. The scintillators are covered with 8mm Pb absorbers to absorb low-energy γ rays. These are harder to discriminate from neutrons than γ rays with higher energies.

Since all the charged particles are stopped in either Microball or in the target chamber, the main issue is to discriminate neutrons from γ rays. Similar to Microball, pulse-shape-analysis techniques are used and the discrimination procedure is described in detail in chapter 4.2.2.

Chapter 4

Data Handling

Fusion-evaporation reactions using Gammasphere in conjunction with Microball and the Neutron Shell are associated with a enormous amount of data signals. A certain fraction of this data, determined by trigger conditions, is written to tape on an event-by-event basis. Data is written in 16384-bytes blocks sub-divided in 16-bit words. In such an experiment a few billion events are written to tape. Since each event typically consists of 50-100 words, the total data written from one experiment corresponds to some 150 Gbyte. In the data analysis this raw data first has to be processed in three steps; compression, presorting and sorting as described below.

4.1 Compression

The raw data from an experiment is first reduced at the same time as we perform consistency checks. The compression procedure was performed using a C-program as follows:

- **Unpack raw data.** Data is unpacked word by word.
- **Remove various events.**
 1. **Consistency checks.** For example, both the time and energy signal of the individual Ge detectors has to be present. Incomplete sets of signals are removed.
 2. **Missing information.** Events that do not fulfil certain conditions, e.g., have at least one valid Ge detector, or events which have irregular information, are removed.
 3. **Unnecessary data.** Some information is only used for redundancy checks and is not necessary for further processing.
- **Rearrange and repack data.** The unpacked data is rearranged and repacked in such a way that the amount of tape storage is reduced by more than a factor of two.

4.2 Presorting

In the presorting process the major part of the data handling takes place:

- **Gain matching of Ge detectors.** Due to a $\sim 0.5 \mu\text{s}$ 10^+ isomer in ^{54}Fe these residual nuclei will be stopped in the Microball absorbers before the transitions below the isomer are emitted. These transitions, with energies between 146 keV and 3.4 MeV, are gain matched for each Ge detector using a second degree polynomial function.
- **Aligning Ge times and defining prompt and delayed γ -ray transitions.** Ge times are aligned and the prompt γ -ray transitions are defined using a two-dimensional gate in a Ge-time vs. Ge-energy matrix. Delayed γ -rays are defined by time gates next to the prompt time peak.
- **Aligning Microball and Neutron Shell signals.** For example, energy and time signals from Microball and the Neutron Shell detectors are aligned throughout the experiment.
- **Particle identification.** See below.
- **Suppression of false two-neutron events.** See below.
- **Event-by-event Doppler correction.** See below.
- **Finally highly compressed data is written to tape or disc separated by certain particle conditions, i.e., reaction channels.**

4.2.1 Proton- α discrimination

An efficient evaporated particle identification is crucial for the study of nuclei following a fusion-evaporation reaction. The main task of Microball is to detect evaporated charged particles and provide a possibility for particle discrimination. The discrimination technique uses pulse-shape-analysis methods. The signal from a Cs(I) crystal has two components; a fast component with a $0.7 \mu\text{s}$ decay time and a slow component with a $7 \mu\text{s}$ decay time. α particles have a larger fraction of the signal in the fast component than protons have, and by differentiating and integrating the signals different quantities are obtained which are used to discriminate α particles from protons. For a more detailed description of particle identification in Microball see Ref. [27].

4.2.2 Neutron- γ discrimination

The major task of the Neutron Shell is to detect neutrons and discriminate them from γ -rays. The neutron discrimination in the Neutron Shell is done in two steps. A rough hardware pre-discrimination is obtained on-line by letting the beam pulse signal veto the prompt γ -ray flash in the neutron detectors. A more sophisticated discrimination is performed off-line. In both cases pulse-shape-analysis techniques are used.

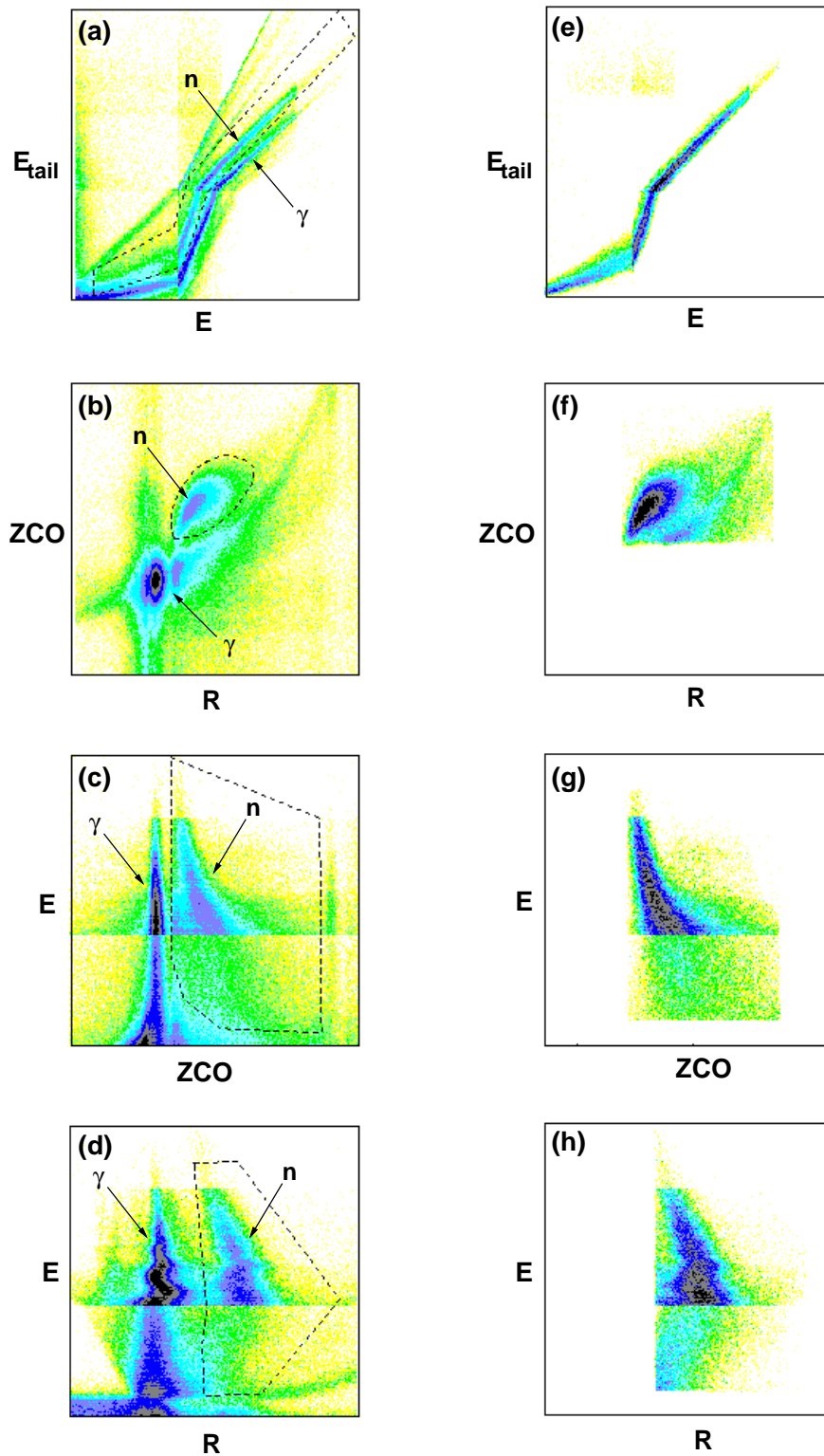


Figure 4.1: Two-dimensional spectra from the Neutron Shell detector 5. Panels (a)-(d) are raw spectra and dashed-line closed contours indicate gate conditions. Panels (e)-(h) are spectra obtained from gate conditions from the three other types of spectra. See text for details.

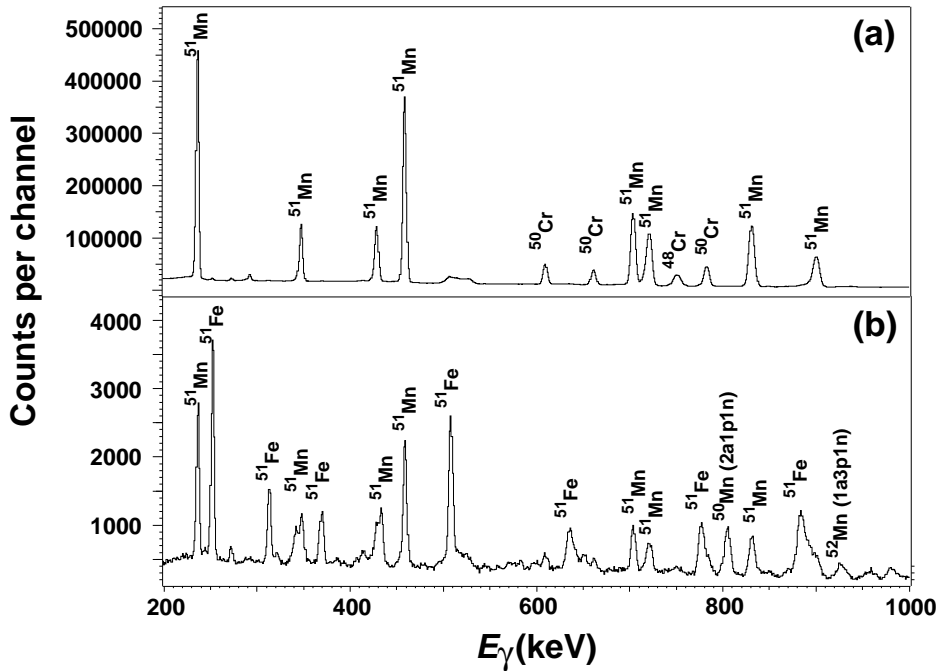


Figure 4.2: Panel (a) shows a γ -ray spectrum gated with two α -particles, and panel (b) shows a spectrum gated with two α -particles and one neutron.

The signals from a liquid scintillator look different for neutrons and γ rays. Neutrons create more scintillator light output in the delayed component of the signal than the γ rays. The signals are differentiated and the zero-cross-over-time (ZCO) is determined. ZCO is the time between a given reference, which in our case is the beam pulse, and the point where the differentiated signal crosses the time axis. In this way the ZCO will occur earlier for γ rays than for neutrons. The total energy E deposited in the detector is determined by integrating the signal over a fixed time window. The third parameter used is the tail energy E_{tail} , which is determined by integrating the signal in a delayed time window. E_{tail} will be larger for neutrons than for γ rays for the same total energy E . We also define the ratio $R = E_{tail}/E$. Figure 4.1 shows eight two-dimensional spectra from the fifth detector of the Neutron Shell. The spectra in the left column are the raw spectra (without any gate conditions) and the dashed-line closed contours are the final gates for neutrons. Note that the binning of E and E_{tail} is different for different spectral regions to keep a balance between sufficient resolution and spectra size.

Spectra in the right column are the results when the gating conditions for the three other spectra are fulfilled. For example, spectrum (e) is obtained when the gating conditions in spectra (b),(c), and (d) are fulfilled. This is an iterative procedure and a compromise between identification efficiency and γ -neutron misidentification has to be done. A neutron-detector event which fulfils all four gate conditions is taken as a neutron. Figure 4.2(a) shows a spectrum gated on two α -particles. This is as close as we would get without neutron detectors, if we want to study ^{51}Fe , which is populated via the $2\alpha 1n$ channel. Figure 4.2(b) shows the enhancement of the ^{51}Fe lines if we use neutron detectors and the discrimination procedure described above. The difference is obvious. In Fig. 4.2(a) we can barely see any transitions from ^{51}Fe , while in

Fig. 4.2(b) transitions from ^{51}Fe are dominating. The contamination from ^{51}Mn in Fig. 4.2(b), which is populated via the $2\alpha 1p$ channel, is due to three effects. First because of a small target impurity of ^{29}Si , which results in the $^{29}\text{Si}(^{32}\text{S}, 2\alpha 1p 1n)^{51}\text{Mn}$ reaction where we fail to detect the evaporated proton. Secondly due to insufficient neutron- γ discrimination and finally γ rays depopulating isomers in the ns regime, e.g., the $17/2^-$ isomeric state in ^{51}Mn , can be interpreted as neutrons.

4.2.3 Suppression of false two-neutron events

False two-neutron events are rather common using neutron-detector arrays such as the Neutron Shell. This is a problem since these events, which are due to neutron scattering, are contaminating $2n$ -gated spectra. There exist, however, methods to suppress them. First we realise that in false two-neutron events the neutron detectors which fire are often immediate neighbours. By interpreting such events as one-neutron events we will suppress the number of false two-neutron events dramatically. However, the number of real two-neutron events will also be reduced. If we assume that the number of real two-neutron events are distributed equally between different detector pairs and that every Neutron Shell detector on average has 5 closest neighbours then $5/30 \sim 17\%$ of all real two-neutron events will be removed. In practice the closest neighbour suppression is, however, necessary to attribute γ rays to the extremely weak $2n$ channels. In principle we can go further and reinterpret events from pairs of detectors that has unusually many events in coincidence compared to other detector pairs. The degree of suppression depends on what we want to obtain. If we want to identify a previously unknown nucleus populated in a $2n$ channel, it is necessary with a ‘hard’ suppression to obtain as clean $2n$ -gated spectra as possible. On the other hand, if we want to study a nucleus where transitions are already known we may prefer a ‘soft’ suppression to get more statistics for $\gamma\gamma$ -coincidence spectroscopy.

4.2.4 Efficiency of the Neutron Shell

If the neutron efficiency is below 100 % we will, e.g., see γ -ray transitions from the nucleus populated in a $3p 1n$ channel, in this case ^{56}Co , in the $3p$ gated spectrum. This is because we fail to detect the evaporated neutron. The relation between neutron efficiency ϵ_n and intensities of γ rays from ^{56}Co is:

$$R = \frac{I(3p; \gamma \text{ in } ^{56}\text{Co})}{I(3p 1n; \gamma \text{ in } ^{56}\text{Co})} = \frac{1 - \epsilon_n}{\epsilon_n} \quad (4.1)$$

where $I(3p; \gamma \text{ in } ^{56}\text{Co})$ and $I(3p 1n; \gamma \text{ in } ^{56}\text{Co})$ are the intensities of γ -ray transitions belonging to ^{56}Co in the $3p$ and $3p 1n$ -gated spectra, respectively. After rearranging we get

$$\epsilon_n = \frac{1}{1 + R} \quad (4.2)$$

The ratio was measured to $R=1.27(8)$ which gives $\epsilon_n^{trig} = 0.44(2)$. However, in this experiment data was written to tape only if four γ rays or three γ rays and one neutron were detected in coincidence, which means that the obtained efficiency is

biased by the trigger condition. The reason that the triggered neutron efficiency is not unity, is that neither the hardware nor the software γ -neutron discrimination is perfect. To get the true unbiased efficiency ϵ_n we have to consider only data which have four or more γ rays in coincidence. In this way the obtained neutron efficiency is independent of trigger conditions. This gives $R=3.36(3)$ and we now obtain $\epsilon_n = 0.23(1)$.

The triggered $2n$ efficiency is now easily obtained as $\epsilon_{2n}^{trig} = \epsilon_n^{trig} \epsilon_n = 0.10(1)$. However, since we have reduced the number of real two-neutron events, the real efficiency will be suppressed with a factor X . In a similar way as above we define

$$R_{2n} = \frac{I(3p2n; \gamma \text{ in } ^{55}\text{Co})}{I(3p1n; \gamma \text{ in } ^{55}\text{Co})} = \frac{\epsilon_n^{trig} \epsilon_n X}{\epsilon_n^{trig} (2 - \epsilon_n^{trig} - \epsilon_n)} \quad (4.3)$$

Using the efficiencies above and the measured value $R_{2n} = 0.058(4)$ we obtain $X = 0.34(2)$ and $\epsilon_{2n}^{trig} = \epsilon_n^{trig} \epsilon_n X = 0.034(2)$. This means that in the suppression of false two-neutron events we remove 66 % of the real two-neutron events. This may sound a lot, but one should remember that this suppression is very ‘hard’ and performed with the intention of identifying previously unknown nuclei populated via $2n$ channels. Once they are identified we can relax the suppression to include only closest neighbours and get a suppression factor $X \sim 83$ % and $\epsilon_{2n}^{trig} \sim 0.083$.

4.2.5 The event-by-event reconstruction method

The energy resolution of the γ -ray peaks is worsened due to the reaction kinematics of fusion-evaporation reactions. This is due to the Doppler shift of the emitted γ rays expressed as

$$E_{\gamma,lab} = E_{\gamma}(1 + \beta \cos\theta) \quad (4.4)$$

where $E_{\gamma,lab}$ is the measured γ energy and E_{γ} is the transition energy. $\beta = \frac{v}{c}$ is the velocity of the residual nuclei and θ is the position of the Ge detector. Finite opening angles of Ge detectors, finite target thickness, and the effect of evaporated particles induce uncertainties in θ and β which causes an uncertainty in $E_{\gamma,lab}$. The contribution of finite opening angles and finite target thickness can be estimated from the derivative of Eq. 4.4:

$$\begin{aligned} \Delta E_{\gamma,lab} &= E_{\gamma} \cos\theta \Delta\beta \\ \Delta E_{\gamma,lab} &= E_{\gamma} \beta \sin\theta \Delta\theta \end{aligned} \quad (4.5)$$

A simple Doppler correction can be obtained using

$$E_{\gamma,corr} = \frac{E_{\gamma,lab}}{1 + \langle\beta\rangle \cos\theta} \quad (4.6)$$

The average recoil velocity $\langle\beta\rangle$ is determined by adjusting it in the computer code until the best energy resolution is obtained in the sum of Ge spectra taken at different angles θ . Typical estimated values for the $^{32}\text{S} + ^{28}\text{Ni} \rightarrow ^{60}\text{Zn}^*$ reaction at 125 MeV beam energy employing a 0.5 mg/cm² thick Si target are; $\langle\beta\rangle = 0.043$ and $\Delta\beta = 0.002$. The effective opening angles of the Gammasphere Ge detectors are approximately $\Delta\theta = 5^\circ$. At a γ energy of 1500 keV using Eq. 4.5 and Eq. 4.6, this would give a

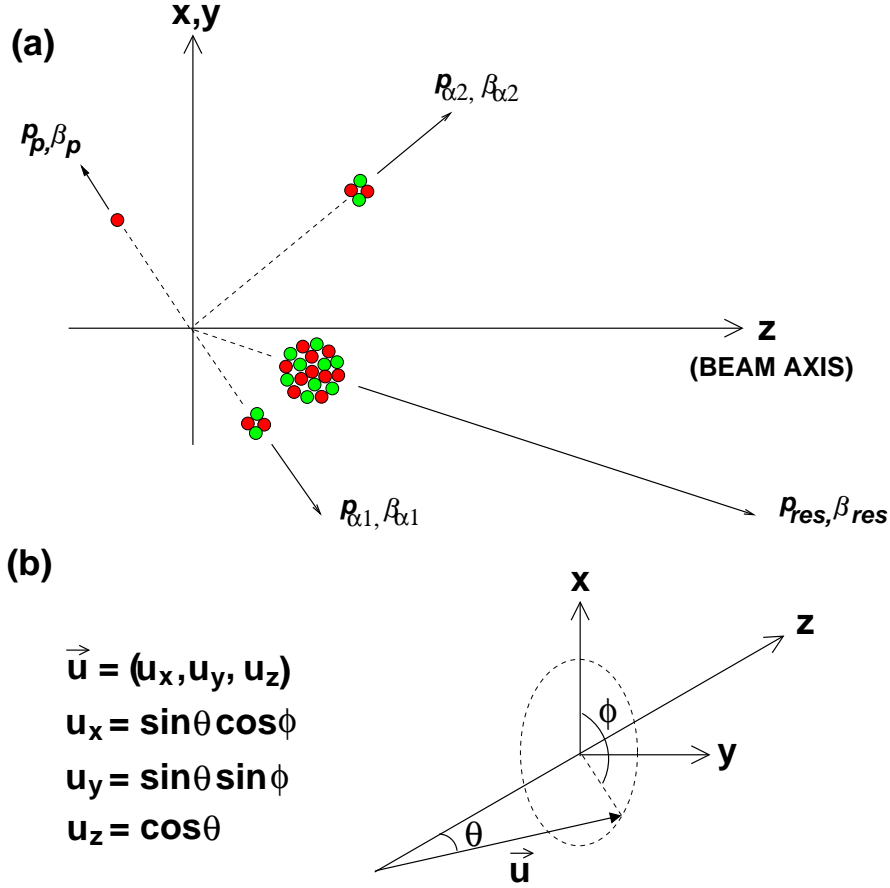


Figure 4.3: Panel (a) shows an event where a compound nucleus evaporates two α -particles and one proton to form a residual nucleus, and panel (b) relates polar and azimuth angles with vector components.

total energy resolution (FWHM) of 10.5 keV, where the intrinsic resolution of the Ge detectors contributes with 2.6 keV, and the uncertainties in β and θ contributes with 2.5 keV and 9.5 keV, respectively. In the calculations we used $\text{FWHM}=2\Delta E_{\gamma,lab}$ and the energy resolution is weighted over the number of detectors and detector angles used in the Gammasphere experiment. As seen from the calculations above the opening angles of the Ge detectors contributes the most. Note that the energy resolution calculated above is only a rough estimate and that the effect of evaporated particles is not taken into account.

To take this effect into account a more sophisticated Doppler correction is required [28]. Evaporated particles carry momentum and the residual nuclei will not necessary recoil in the beam direction z . This is illustrated in Fig. 4.3(a). Since the evaporation of particles is of a statistical nature this effect will also induce a Doppler broadening because of the spread in β and θ . But since we measure the kinetic energies of the evaporated particles in the laboratory system T_i and the direction, this can partly be corrected for by using an event-by-event reconstruction method. If the mass of the evaporated particle is m_i , the magnitude of its momentum becomes

$$p_i = \sqrt{2T_i m_i c^2} \text{ [MeV/c]} \quad (4.7)$$

According to Fig. 4.3(b) the x , y and z components of the momentum are given by

$$\begin{aligned}
p_{i,x} &= p_i \sin\theta_i \cos\phi_i \\
p_{i,y} &= p_i \sin\theta_i \sin\phi_i \\
p_{i,z} &= p_i \cos\theta_i
\end{aligned} \tag{4.8}$$

where θ_i and ϕ_i are the polar and azimuth angles of the particle detectors, respectively. From momentum conservation we know that the momentum of the beam, p_{beam} , equals the momentum of the residual nuclei, p_{res} , plus the momentum of the evaporated particles. Summing up $p_{i,x}$, $p_{i,y}$ and $p_{i,z}$ of the evaporated particles from one event, gives the velocity components and the total velocity of the residual nuclei with mass M_{res}

$$\begin{aligned}
\tilde{\beta}_{res,x} &= -\sum_i p_{i,x}/M_{res}c^2 \\
\tilde{\beta}_{res,y} &= -\sum_i p_{i,y}/M_{res}c^2 \\
\tilde{\beta}_{res,z} &= (\sqrt{2T_{beam}M_{beam}c^2} - \sum_i p_{i,z})/M_{res}c^2 \\
\tilde{\beta}_{res} &= \sqrt{\tilde{\beta}_{res,x}^2 + \tilde{\beta}_{res,y}^2 + \tilde{\beta}_{res,z}^2}
\end{aligned} \tag{4.9}$$

where T_{beam} and M_{beam} is the kinetic energy and mass of the beam nuclei, respectively. Equation 4.9 is true if we use an infinite thin target. This is, however, never the case. We must also consider the energy loss of the recoiling nucleus in the target. In principle, this requires knowledge of the interaction point in the target for every event. This is impossible and we assume that the interactions on average take place in the middle of the target. The energy loss in a Si target for nuclei in the $A \sim 60$ region can be estimated from an equation parameterised from data from Northcliff and Schilling [29]:

$$E_{loss} = d_{eff}(6.0 + 0.65 Z_{res} + 0.27 Z_{res} T_{res}/A - 4.36 T_{res}/A) \tag{4.10}$$

where d_{eff} is the effective target thickness that the recoiling nucleus sees and is given by

$$d_{eff} = \frac{d}{2} \cdot \frac{\tilde{\beta}_{res}}{\tilde{\beta}_{res,z}} \text{ [mg/cm}^2\text{]} \tag{4.11}$$

The true target thickness is d , and Z_{res} and $T_{res}/A = \frac{1}{2}(M_{res}/A)c^2\tilde{\beta}_{res}^2$ are the proton number and the kinetic energy per mass unit of the residual nuclei, respectively. From the energy loss of the residual nuclei a so-called slowing-down factor s is determined according to

$$s = (T_{res} - E_{loss})/T_{res} \tag{4.12}$$

and we get $\beta_{res,i} = s\tilde{\beta}_{res,i}$, $i = x, y, z$. We now have all the information we need to calculate event-by-event β_{res} and the angle θ_{eff} between the recoiling nucleus and the Ge detectors. The product $\beta_{res}\cos\theta_{eff}$ is given by the scalar product of $\vec{\beta}_{res}$ and the unitary vector describing the direction to the Ge detector $\vec{e} = (\sin\theta_{Ge}\cos\phi_{Ge}, \sin\theta_{Ge}\sin\phi_{Ge}, \cos\theta_{Ge})$ and is used instead of $\langle\beta\rangle\cos\theta$ in Eq. 4.6. The free parameters to be adjusted until lowest possible energy resolution is obtained are T_{beam} and d in Eqs. 4.9 and 4.11, respectively. A $2\alpha 1p$ -gated spectrum

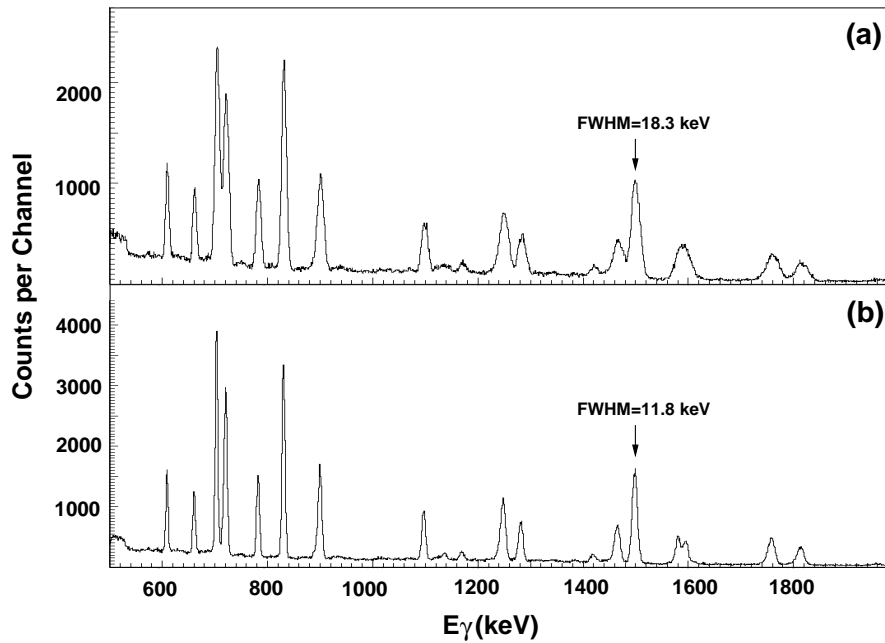


Figure 4.4: Panel (a) shows a $2a1p$ -gated spectrum obtained with an averaged Doppler correction using $\langle\beta\rangle=0.043$. Panel (b) shows a $2a1p$ -gated spectrum obtained with the event-by-event reconstruction method. Notice the reduction in FWHM for the 1500 keV γ -ray transition in panel (b). See text for details.

obtained with the event-by-event reconstruction method described above is seen in Fig. 4.4(b) and compared to a spectrum obtained with an averaged Doppler correction using $\langle\beta\rangle=0.043$ in Fig. 4.4(a). As seen in the figure the energy resolution is improved by a factor ~ 1.5 .

4.3 Sorting

In the sorting procedure the presorted data is processed in various programs to:

- **Generate 1D spectra.**
- **Sort data into $\gamma\gamma$ matrices.**
- **Sort data into $\gamma\gamma\gamma$ correlation cubes.**
- **Apply additional TE conditions.**

4.3.1 TE gating

We have described how the detection of evaporated particles following a fusion-evaporation reaction can be used to impose gating conditions in two-dimensional spectra and study γ rays in coincidence. There is yet another method to further clean the particle-gated spectra. This is the so called total-energy (TE) gating method [30]. The method uses the fact that the excitation energy E^* is (nearly) a constant. By removing the Heavimet absorbers we can measure the sum-energy of the γ rays, H , and the γ -ray multiplicity, K [31]. The total energy detected from one event is then $H + P$, where P is the sum of the measured particle energies. $H + P$ is proportional to the excitation energy. Figure 4.5 shows two-dimensional spectra used for TE gating. Spectra (a) and (c) show events in the $2\alpha 1p$ channel (where ^{51}Mn is populated) in coincidence with two γ -ray transitions from ^{51}Mn . Spectra (b) and (d) show contaminating events in the same channel that are double gated on transitions from ^{50}Cr . The only way for events from ^{50}Cr (populated in the $2\alpha 2p$ channel) to end up in the $2\alpha 1p$ channel is if we fail to detect or identify one proton. In both cases we are missing the energy from this proton. If we study Fig. 4.5 we see that events from ^{50}Cr on average have lower P and $H + P$ than events from ^{51}Mn . By putting gate conditions optimised for ^{51}Mn , indicated by dashed-line solid-contours in the figure, we can eliminate a large fraction of the ^{50}Cr events in the $2\alpha 1p$ spectrum. This is seen in Fig. 4.6. We see from the figure that not only the peaks from ^{50}Cr are reduced, but also the background.

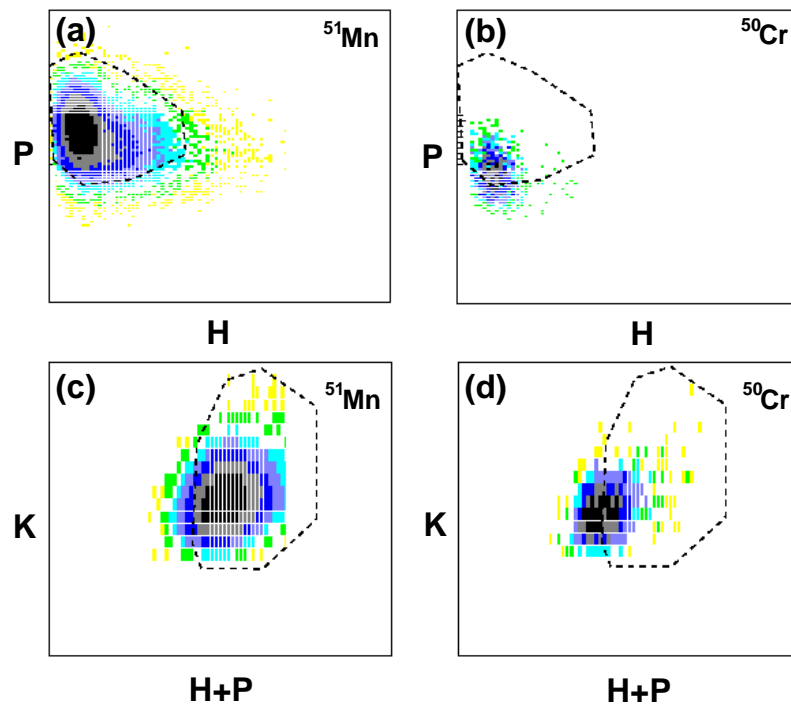


Figure 4.5: Two-dimensional spectra used for TE gating. Spectra (a) and (c) show events double gated on γ -ray transitions in ^{51}Mn . Spectra (b) and (d) show events double gated on transitions in ^{50}Cr . Dashed-line contours are gating conditions for the ^{51}Mn setting. See text for details.

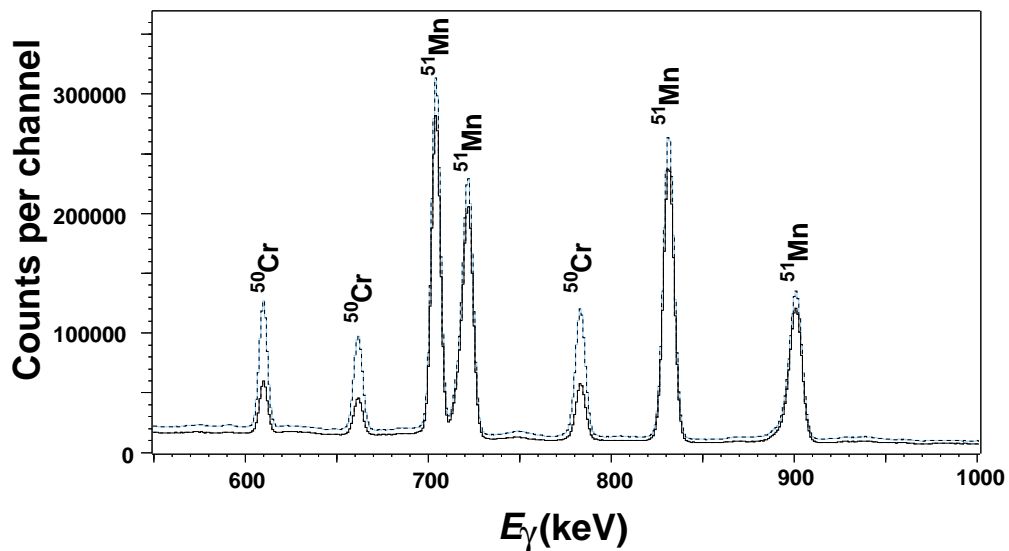


Figure 4.6: Spectrum obtained without TE gating (dashed line) and spectrum obtained with TE gating (solid line).

Chapter 5

Data Analysis

5.1 Coincidence Spectroscopy

When constructing level schemes including a lot of transitions it is useful to sort particle- and TE -gated data in E_γ - E_γ matrices and E_γ - E_γ - E_γ cubes. By performing γ -energy gates on one axis in a E_γ - E_γ matrix we can study the γ rays in coincidence. Figure 5.1 shows an example. Panel(a) shows the γ -ray spectrum resulting from the γ -energy gate at the 369 keV γ -ray transition in the E_γ - E_γ matrix gated by two α -particles and one neutron, which corresponds to the residual nucleus ^{51}Fe . We see that several transitions are in coincidence with the 369 keV line. To continue we set a γ gate around 1433 keV with the resulting coincidence spectra shown in Fig. 5.1(b). From the two spectra we conclude that the 369 keV and 1433 keV lines are in coincidence with several transitions at the same energy, but also that there are transitions in one gate which are not present in the other. This implies, e.g., that the 1433 keV and 1754 keV transitions are parallel, and similar that the 369 keV and 1262 keV transitions are parallel. This assignment is supported by the 321 keV transition which together with the 1433 keV line adds up to 1754 keV and the 369 keV and 893 keV lines sum up to 1262 keV. Continuing in this way we can construct the level scheme for ^{51}Fe shown in Fig. 5.1(c).

The relevant part of a new extensive level scheme of the mirror partner ^{51}Mn [32] is shown in Fig. 5.1(d). Note the great similarities of the two level schemes. This feature of mirror nuclei together with sum-energy arguments discussed above could in fact be used to construct the level scheme of ^{51}Fe without involving coincidence spectroscopy at all.

5.2 Spin and Parity Assignment of Nuclear States

Spin and parity assignments of nuclear states are very important for the understanding of the underlying physics. The assignments to nuclear ground states are often based on β -decay measurements and from there we can deduce spin and parities of excited states by studying connecting γ -ray transitions.

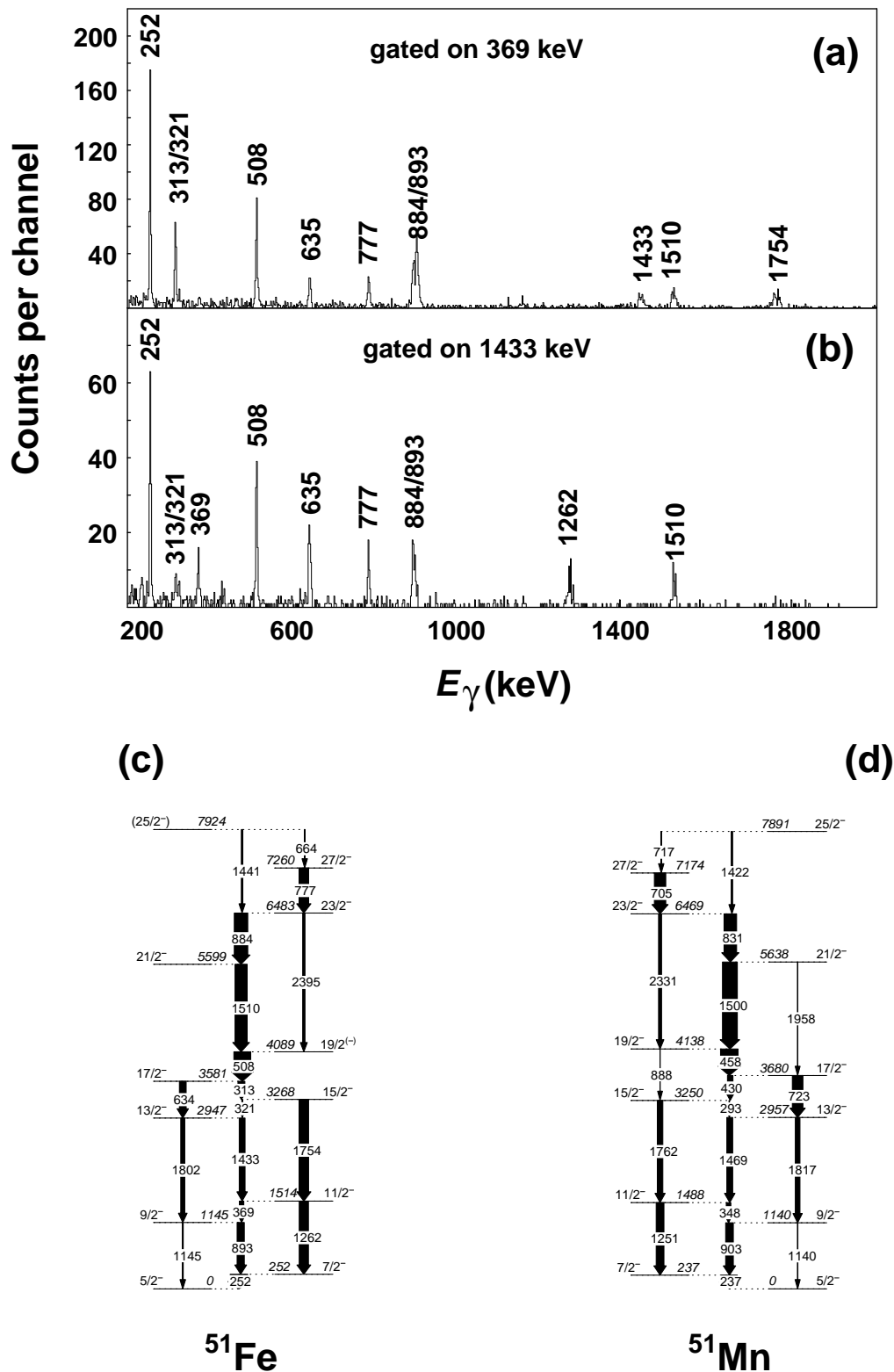


Figure 5.1: Panels (a) and (b) show $2\alpha 1n$ -gated spectra in coincidence with the 369 keV line and 1433 keV line, respectively. Panel (c) and (d) show the relevant parts of the level schemes of ^{51}Fe and ^{51}Mn , respectively. See text for details.

5.2.1 Electro magnetic transitions

Assume a γ -ray transition from an initial nuclear state with angular momentum \vec{I}_i to a final state with angular momentum \vec{I}_f . If we denote the angular momentum of the γ ray with \vec{L} the conservation of angular momentum gives

$$\vec{I}_i = \vec{L} + \vec{I}_f \quad (5.1)$$

The multipolarity L is thus given by the following selection rule

$$|I_i - I_f| \leq L \leq |I_i + I_f| \quad (5.2)$$

The exception to this selection rule occurs when $\vec{I}_i = \vec{I}_f$. Since there are no monopole ($L = 0$) transitions in which a single photon is emitted we have $L \neq 0$. The parity of the radiation field depends on both the multipolarity and the character of the field. Whether or not a γ -ray transition is parity conserving is given by the following rules

$$\begin{aligned} \text{parity conserving :} & \quad \text{electric even } L, \text{ magnetic odd } L \\ \text{parity breaking :} & \quad \text{electric odd } L, \text{ magnetic even } L \end{aligned} \quad (5.3)$$

If we know the spin and parity for one nuclear state, we can determine the spin and parity of other nuclear states by deducing the multiplicities and characters of the connecting γ -ray transitions. A transition can be pure and stretched, that is $L = I_i - I_f = \Delta I$, or mixed. In the latter case the transition has contributions also from higher multiplicities. The degree of mixing is given by the transitional mixing ratio δ according to

$$\delta = \frac{\langle I_f | M(T_2 L_2) | I_i \rangle}{\langle I_f | M(T_1 L_1) | I_i \rangle} \quad (5.4)$$

where $\langle I_f | M(TL) | I_i \rangle$ is the matrix element of the operator $M(TL)$ which besides from changing the nuclear state from $|I_i\rangle$ to $|I_f\rangle$ also creates a photon of the proper multipole order L and character T . Since we choose $L_2 > L_1$ a stretched transition will always have $\delta = 0$.

5.2.2 Spin assignment of nuclear states

Since γ -rays carry angular momentum the γ -ray transitions are associated with angular distributions given by the spherical harmonics. To perform meaningful measurements of angular distributions, without using coincidence methods, we require a mechanism that aligns \vec{I}_i in the γ -emitting nuclei. In the fusion-evaporation reaction angular momentum is induced to the residual nucleus with the vector lying in a plane perpendicular to the beam axis. This spin alignment is however, somewhat destroyed from the effect of evaporated particles, the emittance of γ rays and the presence of isomeric states. By detecting the γ -ray of interest in different polar angles we obtain an angular distribution from which the multipolarity is deduced. In Fig. 5.2 typical high-spin fully aligned angular distributions for a $\Delta I = 1$ and a $\Delta I = 2$ transition is seen. It is also possible to deduce the mixing ratio of the transition. Care should be taken here since for a given distribution there is almost always

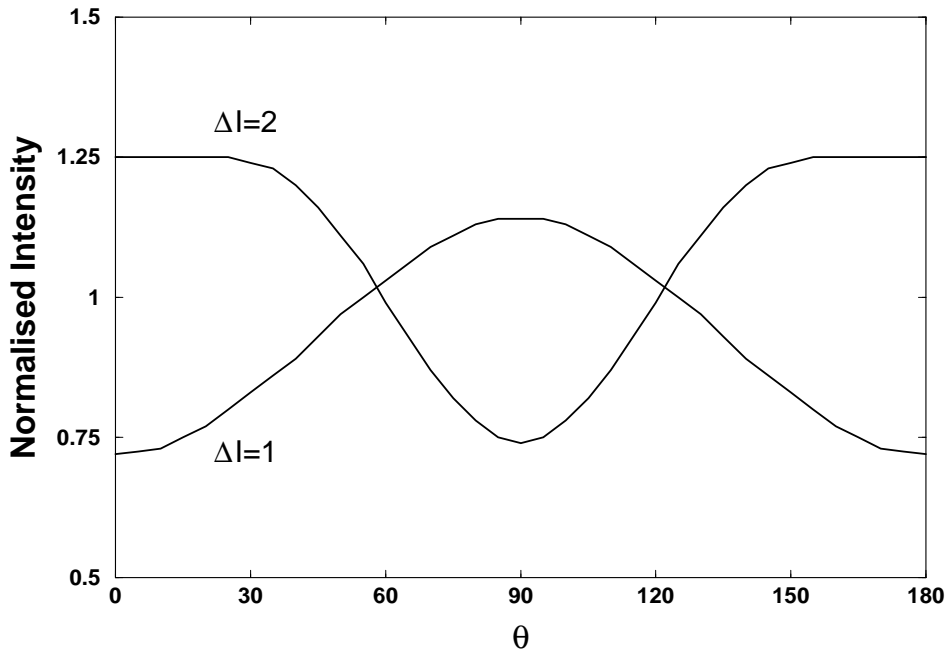


Figure 5.2: Typical high-spin angular distributions for a $\Delta I = 1$ and a $\Delta I = 2$ transition. Note that the angular distributions are symmetric around $\theta = 90^\circ$.

two possible solutions for the mixing ratio, δ . What is often used for multipole assignments is the so-called ratio of yields given by

$$R_{30-83} = \frac{I(\gamma \text{ at } 30^\circ)}{I(\gamma \text{ at } 83^\circ)} \quad (5.5)$$

Of course, any combination of angles can be used as long as the ratio is sensitive enough. Assuming a realistic spin alignment, we get for observed stretched $\Delta I = 2$ transitions $R_{30-83} \approx 1.2$, and for stretched $\Delta I = 1$ transitions $R_{30-83} \approx 0.8$.

Studying the angular distributions of two subsequent transitions there is an angular correlation between them because the final state of the first transition is the initial state of the second transition. What is often deduced is the ratio of directional correlations of oriented states (DCO-ratio) [33], which is for example given by

$$R_{DCO}(30-83; \gamma_1, \gamma_2) = \frac{I(\gamma_1 \text{ at } 30^\circ; \text{gated with } \gamma_2 \text{ at } 83^\circ)}{I(\gamma_1 \text{ at } 83^\circ; \text{gated with } \gamma_2 \text{ at } 30^\circ)} \quad (5.6)$$

In general known stretched $E2$ transitions are used for gating. In this case we expect $R_{DCO} \approx 1.0$ for stretched $\Delta I = 2$ transitions and $R_{DCO} \approx 0.6$ for stretched $\Delta I = 1$ transitions.

5.2.3 Parity assignment of nuclear states

To deduce parities of nuclear states we must also determine the character of the connecting transitions. The most efficient method is to measure the polarisation of γ -rays. Assuming spin alignment this method uses the fact that γ rays undergo Compton scattering and that the direction of the Compton scattered γ -ray depends on the character of it. This method can make use of segmented detectors, which are

available in both Euroball and Gammasphere.

If polarisation measurements are not possible we have to rely on indirect methods. It turns out that transitions with electric character is about 100 times more probable than transitions with magnetic character for a given multipolarity. If we assume that the lowest permitted multipole often dominates we can conclude that parity breaking $\Delta I = 1$ and parity conserving $\Delta I = 2$ transitions are most likely to be stretched $E1$ and $E2$ transitions, respectively. Using these arguments observed $\Delta I = 1$ transitions with significant mixing are most certainly mixed $E2/M1$ transitions.

Another example of indirect parity assignment is finally given. If we for example identify a rotational structure we can at least tentatively assign the transitions to be stretched $E2$ transitions. If we in addition can deduce spin and parity of at least one of the states in the structure we can tentatively assign spin and parities for the whole structure.

Chapter 6

Conclusions and Outlook

Excited states in the $T_z = -1/2$ nucleus ^{51}Fe were identified for the first time. The level scheme includes 18 previously unknown γ -ray transitions and reaches the fully aligned $I^\pi = 27/2^-$ terminating state of the five holes in the $1f_{7/2}$ shell. The $17/2^-$ state was found to be isomeric and the lifetime was measured to $2.87_{-0.11}^{+0.09} \pm 0.43$ ns. The $T_z = +1/2$ mirror partner ^{51}Mn was previously known up to the terminating $27/2^-$ state. The mirror symmetry of ^{51}Fe and ^{51}Mn is discussed and the general features of the CED diagram can be explained by the breaking and aligning of proton pairs. The CED diagram is well reproduced by large-scale shell-model calculations [34] and further improved by the decomposition of the Coulomb interaction in a monopole part and a multipole part [19].

Previously the study of mirror nuclei has been restricted to the comparison of level energies. Although CED diagrams of mirror nuclei reveal a lot of interesting physics much more can be learned if we also include studies of electromagnetic decay properties, such as lifetimes of excited states and transitional mixing ratios. To give an example we deduced the $B(E2)$ values for the $17/2^- \rightarrow 13/2^-$ transitions in both ^{51}Fe and ^{51}Mn to be $0.12(2)$ W.u. To see how the $B(E2; 17/2^- \rightarrow 13/2^-)$ ratio depends on the effective proton charge ϵ_p we performed simple shell-model calculations and the result is shown in Fig. 6.1(a). The calculation is performed with the restriction that $\epsilon_p + \epsilon_n = 2$ where ϵ_n is the effective neutron charge. As seen in the figure there is a rather weak dependence and we cannot say anything about the effective proton charge in this case. We also investigated how the $B(E2; 27/2^- \rightarrow 23/2^-)$ ratio depends on ϵ_p and the result is shown in Fig. 6.1(b). Here we see a much stronger dependence but unfortunately we miss experimental values to compare to, since the lifetime of the $27/2^-$ state in ^{51}Fe is unknown. The lifetime of the analogue state in ^{51}Mn is known to be $130(3)$ ps. A future experiment dedicated to measure the lifetime of the $27/2^-$ state in ^{51}Fe would therefore be interesting as it could provide us with valuable data on effective charges in the $1f_{7/2}$ shell. In a similar way as with the $B(E2)$ ratios we can also study differences in mixing ratios of dipole transitions in the $A = 51$ mirror nuclei which should be able to tell us something about effective g -factors (see paper 2 in this thesis). With the full statistics from the two experiments that this work is based on we hope to perform extended mirror symmetry studies of this kind. Another interesting aspect would be if we could identify core excited states in ^{51}Fe and compare these to analogue states in the recently extended level scheme of ^{51}Mn [32]. This would not only be interesting from mirror symmetry

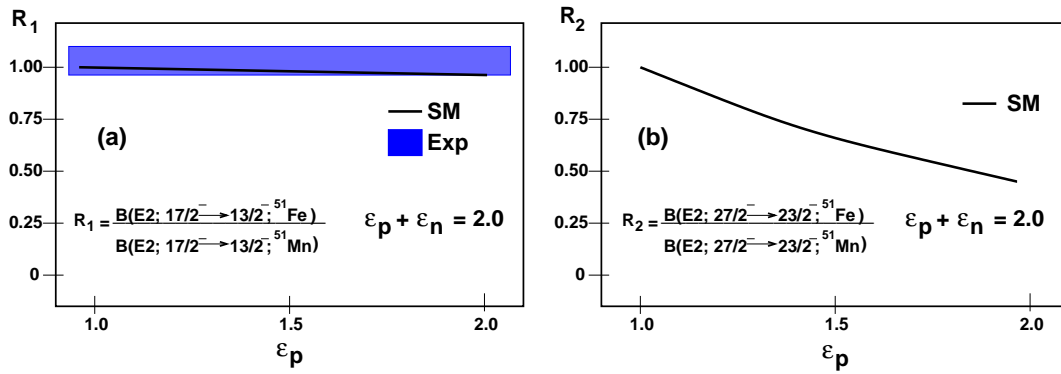


Figure 6.1: Theoretical and experimental $B(E2)$ ratios as a function of effective proton charge. SM stands for Shell-Model calculations. See text for details.

but may also probe differences in single-particle energies for neutrons and protons in the upper fp -shell.

The identification of excited states in the $T_z = -1$ nucleus ${}^{54}\text{Ni}$ is also a future challenge. This would complete the spectroscopic information in the $A = 54$ $T = 1$ isobaric triplet. It would be of special interest since the comparison of excited states in ${}^{54}\text{Ni}$ and the $T_z = +1$ ${}^{54}\text{Fe}$ nucleus would provide us with a set of experimental Coulomb matrix elements valid for the upper $1f_{7/2}$ shell to be used in shell-model calculations. In addition, the possibility of measuring the lifetime of the 10^+ state in ${}^{54}\text{Ni}$ and compare this to the known lifetime $\tau = 525(10)$ ns of the analogue state in ${}^{54}\text{Fe}$ will give us additional information on effective charges and the stiffness of the ${}^{56}\text{Ni}$ core with respect to quadrupole shape changes [35].

The continuation of experimental studies of mirror nuclei such as these discussed above together with on-going theoretical achievements will certainly extend our knowledge in this interesting field of nuclear structure physics.

Acknowledgements

First, I would like to thank my supervisors Claes Fahlander, for introducing me to the interesting field of nuclear physics and for giving me the opportunity to join his group, and Dirk Rudolph, for sharing his knowledge and experience in nuclear physics. Their professional and friendly guidance throughout this work is greatly appreciated.

I also thank the rest of the Nuclear Structure Group in Lund, Hans Ryde, Margareta Hellström, and Milena Mineva, for providing a nice working atmosphere and many interesting discussions. Especially, I thank Corina Andreoiu for all the good laughs we shared and for making each day at work more enjoyable.

Fruitful discussions on various nuclear structure phenomena together with the Mathematical Physics group during “nuclear coffee” are also acknowledged.

Finally, I am grateful to my family for always being there, and most of all, to Maria, for her love and support.

References

- [1] J. Chadwick, *Nature*, 129:312 (1932).
- [2] J. Chadwick, *Proceedings of the Royal Society, Series A*, **136**, 692 (1932).
- [3] W. Heisenberg, *Z. Phys.* **77**, 1 (1932).
- [4] W. Heisenberg, *Z. Phys.* **78**, 154 (1932).
- [5] W. Heisenberg, *Z. Phys.* **80**, 587 (1933).
- [6] M.A. Bentley *et al.*, *Phys. Lett. B***437**, 243 (1998).
- [7] C.D. O’Leary *et al.*, *Phys. Rev. Lett.* **79**, 4349 (1997).
- [8] P.E. Garrett *et al.*, *Phys. Rev. Lett.* **87**, 4005 (2001).
- [9] S.M. Lenzi *et al.*, *Phys. Rev. Lett.* **87**, 2501 (2001).
- [10] C.D. O’Leary *et al.*, *Phys. Lett. B***525**, 49 (2002).
- [11] H. Junde, *Nucl. Data Sheets* **87**, 507 (1999).
- [12] D. Rudolph *et al.*, *Z. Phys.* **A358**, 379 (1997).
- [13] C.A. Ur *et al.*, *Phys. Rev. C***58**, 3163 (1998).
- [14] K.S. Krane, “*Introductory Nuclear Physics*”, John Wiley & Sons, New York (1988).
- [15] K.L.G. Heyde, “*The Nuclear Shell Model*”, Springer Verlag, Heidelberg (1994).
- [16] S.G. Nilsson, *Dan. Mat. Fys. Medd.* **29**, no. 16 (1955).
- [17] S.G. Nilsson and I. Ragnarsson, “*Shapes and Shells in Nuclear Structure*”, Cambridge University Press (1995).
- [18] J.A. Nolen and J.P. Schiffer, *Ann. Rev. Nuc. Sci.* 19, **471** (1969).
- [19] A.P. Zuker *et al.*, to be published.
- [20] <http://nucalf.physics.fsu.edu/~riley/gamma/>
- [21] EUROBALL III, A European γ -ray facility, Eds. J. Gerl and R.M. Lieder, GSI, (1992).

- [22] I.-Y. Lee , Nucl. Phys. A **520**, 641c (1990).
- [23] <http://wunmr.wustl.edu/~dgs/neutronsshell/index.html/>
- [24] D.G. Sarantites *et al.*, Nucl. Instr. Meth. A **381**, 418 (1996).
- [25] D.G. Sarantites *et al.*, to be published.
- [26] J. Cederkäll *et al.*, Nucl. Instr. Meth. A **385**, 166 (1997).
- [27] C. Andreoiu, “Superdeformation and Prompt Proton Decays in ^{59}Cu ”, Licentiate Thesis, Department of Physics, Lund University (2000).
- [28] D. Seweryniak *et al.*, Nucl. Instr. Meth. A **340**, 353 (1994).
- [29] L.C. Northcliffe and R.F. Schilling, Nucl. Data Tables **7**, 256, (1970).
- [30] C.E. Svensson *et al.*, Nucl. Instr. Meth. A **396**, 228 (1997).
- [31] M. Devlin *et al.*, Nucl. Instr. Meth. A **383**, 506 (1996).
- [32] J. Ekman *et al.*, to be published.
- [33] D. Rudolph *et al.*, Eur. Phys. J. A **4**, 115 (1999).
- [34] A. Poves, J. Sanchez-Solano, E. Caurier and F. Nowacki, Nucl. Phys. A **694**, 157 (2001).
- [35] M. Lipoglavsek, “Rigidity of the Doubly-Magic ^{100}Sn Core”, Ph. D. Thesis, Department of Physics, Lund University (1998).